

Data-driven modeling of fluid flow around rotating structures with graph neural networks

Rui Gao^a, Zhi Cheng^b, Rajeev K. Jaiman^{a,*}

^a*Department of Mechanical Engineering, The University of British Columbia, Vancouver, BC V6T 1Z4*

^b*Department of Mechanical Engineering, University of California, Berkeley, Berkeley, CA 94720*

Abstract

Graph neural networks, recently introduced into the field of fluid flow surrogate modeling, have been successfully applied to model the temporal evolution of various fluid flow systems. Existing applications, however, are mostly restricted to cases where the domain is time-invariant. The present work extends the application of graph neural network-based modeling to fluid flow around structures rotating with respect to a certain axis. Specifically, we propose to apply a graph neural network-based surrogate modeling for fluid flow with the mesh corotating with the structure. Unlike conventional data-driven approaches that rely on structured Cartesian meshes, our framework operates on unstructured co-rotating meshes, enforcing rotation equivariance of the learned model by leveraging co-rotating polar (2D) and cylindrical (3D) coordinate systems. To model the pressure for systems without Dirichlet pressure boundaries, we propose a novel local directed pressure difference formulation that is invariant to the reference pressure point and value. For flow systems with large mesh sizes, we introduce a scheme to train the network in single or distributed graphics processing units by accumulating the backpropagated gradients from partitions of the mesh. The effectiveness of our proposed framework is examined on two test cases: (i) fluid flow in a 2D rotating mixer, and (ii) the flow past a 3D rotating cube. Our results show that the model achieves stable and accurate rollouts for over 2000 time steps in periodic regimes while capturing accurate short-term dynamics in chaotic flow regimes. In addition, the drag and lift force predictions closely match the CFD calculations, highlighting the potential of the framework for modeling both periodic and chaotic fluid flow around rotating structures, and paving the path towards a graph neural network-based surrogate model for more complex scenarios like flow around marine propellers.

Keywords. Graph Neural Networks, Rotating Fluid Flow, Data-Driven Model, Rotation Equivariance

1. Introduction

Rotating structures, including marine and aeronautic propellers, centrifugal pumps and blowers, stirring mixers, wind and gas turbines, etc., comprise an important part of modern machinery. Most of these rotating structures are immersed in fluids, usually air or water, and the fluid flow around such rotating structures is frequently of interest due to their profound impact on the performance and lifespan of machines that include these rotating structures. To improve the understanding of the fluid flow around rotating structures and to facilitate design and control efforts, computational fluid dynamics (CFD) techniques are usually adopted to generate simulations of the flow [1, 2, 3, 4]. However, CFD simulations are computationally heavy, especially when simulating large 3D cases. This limitation leads to challenges in the application of CFD simulations in the iterative design process and real-time model-based flow

*Corresponding author

Email addresses: garrygao@mail.ubc.ca (Rui Gao), chengzhi@berkeley.edu (Zhi Cheng), rjaiman@mech.ubc.ca (Rajeev K. Jaiman)

control. An increasing interest has therefore arisen in the development of cheaper surrogate models that could be adopted for the aforementioned purposes.

Recent rapid development and application of deep learning methods has inspired a series of applications of these models in fluid flow modeling, including the modeling of fluid flow around rotating structures. Existing work includes predicting or fitting fluid field within a pump [5], around a propeller [6, 7], within a stirring mixer [8, 9], around a spinning sphere [10], within a co-rotating disk cavity [11], etc. These works typically adopt either multilayer perceptrons with specific feature design or training loss design or convolutional neural networks. However, it should be noted that most of these works focus on obtaining a prediction of static or time-averaged flow field rather than the spatio-temporal evolution of the flow. One significant exception is the recent work by Li et al. [6] which features time series prediction of the wake after a propeller with a merged convolution-transformer network, despite under a series of limitations: Only the flow in the wake region is predicted, only a 2D slice out of the 3D flow field is predicted, and the authors only report predictions up to 15 time steps – a rather short rollout compared with standard results with 2D cases.

It turns out that the aforementioned limitations in [6] might be due to the choice of the architecture. Neural networks that include convolutional layers can only be applied to structured (and usually also uniform) Cartesian meshes due to the inherent limitation of convolutions, meaning that it is likely impossible to resolve the flow around the surface of a complex object like a propeller without an unaffordable computational burden. Self-attention within a transformer layer computes the *global* correlation between each node within the mesh with every node within the mesh, leading to a computational overhead that increases quadratically with the mesh size, making it rather difficult to apply the model to large 3D cases.

Recently, graph neural networks have been introduced to the modeling of fluid flow. Being able to work with graphs transformed from unstructured mesh, one could easily adopt a body-fitting mesh that is only refined in regions of interest, leading to significant reduction in the mesh size compared to the case with convolutional neural networks while maintaining a satisfactory resolution. This unique advantage has inspired the recent integration of graph neural networks into various fluid flow modeling scenarios. Applications include, but are not limited to, flow around bluff or streamlined bodies [12, 13, 14, 15, 16, 17], fluid-structure interactions [18], particulate suspension [19], reacting flow [20], cavitating flow [21], shock waves [22], and environmental flow above [23] or below [24] the surface of the Earth. For a more comprehensive review of recent advances in the field, the reader is referred to Zhao et al. [25]. Considering the variety of reported applications of graph neural networks, it is reasonable to hypothesize that it will also serve as a proper architecture for modeling fluid flow around rotating structures. Li et al. [26] recently applied a graph neural network to model the flow around a radial turbine. However, similar to previous works using other network architectures, their focus was limited to predicting time-averaged flow fields, without addressing the spatio-temporal dynamics of unsteady flow around rotating structures. They also choose to only model only a single blade of the turbine, which relies on the implicit assumption that the flow is cyclic periodic that can be true for the time-averaged flow field but not for instantaneous flow fields.

In this work, we aim to bridge this gap by developing a rotation-equivariant graph neural network framework capable of modeling the full spatio-temporal evolution of fluid flow around rotating bodies. Specifically, we will propose a rotation equivariant graph neural network framework that operates in polar (for 2D) or cylindrical (for 3D) coordinates that co-rotates with the rotating structure. In addition to this main contribution, we also notice that some fluid systems, especially those in enclosed environments, do not necessarily have a Dirichlet pressure boundary, leading to difficulty in modeling the pressure within the domain with neural networks. We will address such difficulty in this work by modeling local directed pressure differences instead of the pressure itself, and later recover the pressure field in the post-processing steps through the solution of a linear system.

Since graph neural networks usually rely on local connectivity and message passing, the computa-

tional cost of a graph neural network-based model can expect to increase approximately linearly with the mesh size. This property makes GNNs a computationally efficient choice for modeling large-scale 3D fluid systems, especially compared to global architectures like transformers. Recent studies (e.g., [27, 28, 29]) have explored such possibilities with the graph neural network model trained by multiple GPUs that synchronize between themselves during the forward and backward passes of the network. However, single-GPU training strategies for large graph-based fluid simulations remain relatively underexplored. Dupuy et al. [30] briefly mentioned a mesh partitioning approach for surface graphs, but to our knowledge, comprehensive methods for volumetric 3D meshes are lacking.

We extend the partitioning approach by developing a buffer-aware training strategy for hypergraphs derived from 3D meshes. This allows for gradient accumulation across graph segments on a single GPU while preserving training accuracy. We also quantify the memory and computational overhead associated with this approach and demonstrate its effectiveness for large-scale simulations. The proposed graph neural network framework will be assessed in two test cases, namely the flow in a 2D stirring mixer and the flow around a 3D rotating cube. We will demonstrate that the network is able to provide stable and accurate long-term rollout predictions for thousands of time steps for flow in periodic regimes and accurate short-term dynamics for chaotic flow scenarios. These results highlight the ability of graph-based surrogate modeling for fluid flow around rotating bodies and provide a foundation for extending the method to more complex systems such as propellers, turbines, and other real-world applications.

This paper is organized as follows. Section 2 will cover the necessary background and methodology, including the definition of the problem along with its domain and the corresponding coordinate system, the spatio-temporal discretization of the system, as well as the setup of the GNN-based framework. In the following Sec. 3 we lay out the setup of two test cases used to demonstrate the framework, followed by detailed descriptions of how the framework is trained for the two cases. The results of the two test cases will be discussed and compared with the corresponding CFD results in Sec. 4. We will conclude the work in Sec. 5.

2. Methodology

2.1. Fluid flow around rotating structure, co-rotating domain

Consider a domain Ω in which a single or multiple rigid bodies rotating around a fixed axis are immersed in a fluid flow. For computational fluid dynamics (CFD) simulations of such fluid systems, the sliding mesh approach [31] is frequently employed, in which the domain is partitioned into two parts, one static and the other co-rotating with the rigid body. The two parts are connected on their interface, where interpolation is performed between the two parts. For cases where only the flow around the rotating body is of interest, it is frequently possible to include a large enough region in the co-rotating part of the domain such that all the flow physics of interest is contained within that part. We make such assumption in this work, which enables us to discard the less important part of the domain and only focus on a single domain Ω_f with circular (for 2D cases) or cylindrical (for 3D cases) outer boundaries that co-rotates with the rotating body, illustrated in Fig. 1a.

2.2. Rotation equivariance, choice of coordinate system

With the domain of the system and its surrogate model defined, we proceed to define the coordinate system. For the fluid domain defined in the previous Sec. 2.1, it is preferable that a data-driven model of the system satisfies rotation equivariance: if the state of the system at two different instants t_1 and t_2 is exactly the same after being rotated by $\delta\theta = \int_{t_1}^{t_2} \omega(t)dt$ around the axis of rotation of the rigid body Ω_s , then it is expected that the state of the simulated / predicted system at time $t_1 + \delta t$ and $t_2 + \delta t$ should also be exactly the same after the same rotation. Expressed in equations, one could write that if

$$\mathbf{q}^{t_2} = \mathbf{R}_{\delta\theta}(\mathbf{q}^{t_1}) \quad (1a)$$

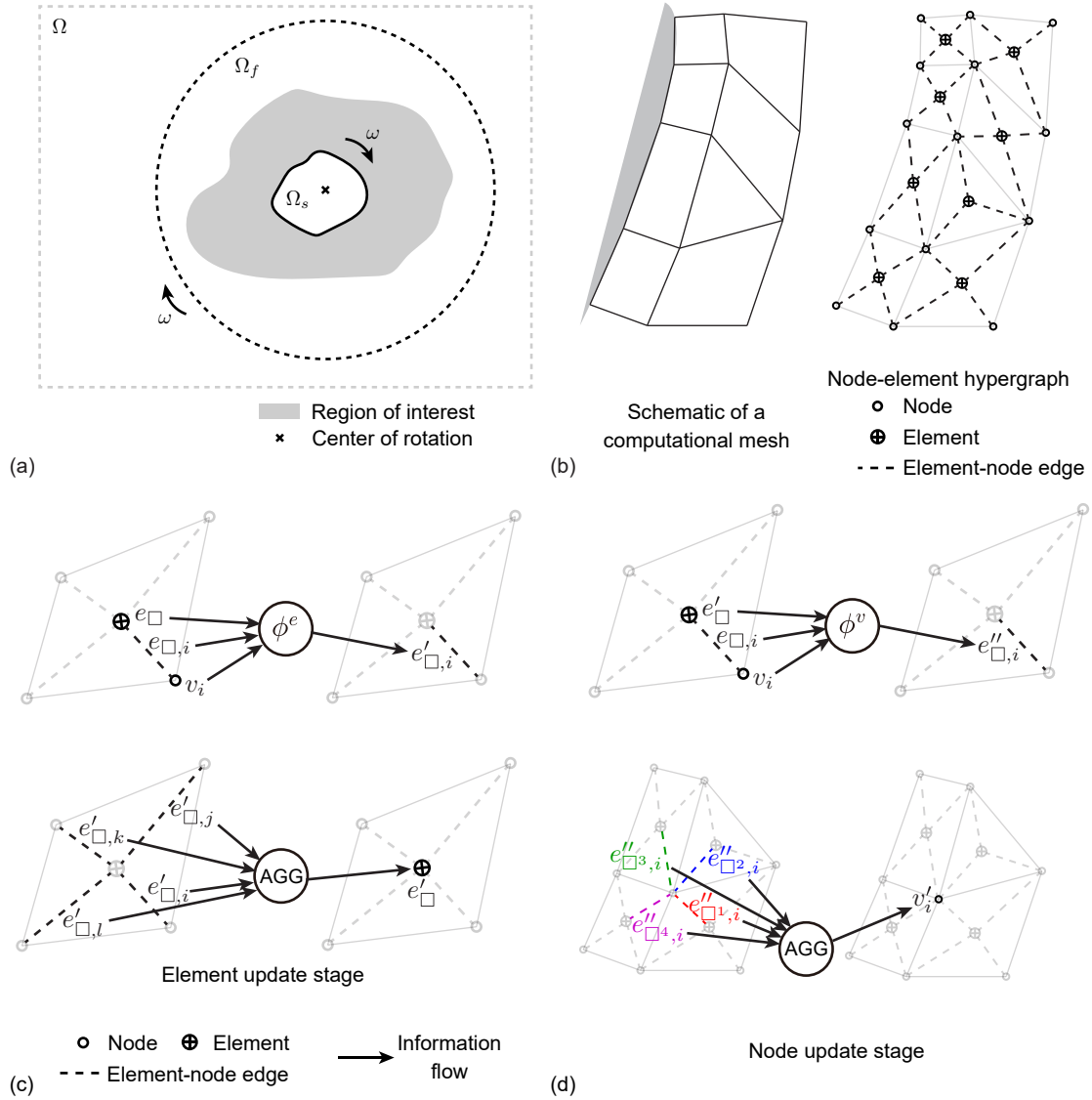


Figure 1: (a) Schematic of the relation between the system domain Ω , fluid domain that is modeled Ω_f , and solid domain Ω_s , (b) conversion from a computational mesh to a node-element hypergraph, and (c) schematic of the element and node update stages within each hypergraph message-passing layer in ϕ -GNN.

then for any time step δt the following equation should also hold

$$\mathbf{q}^{t_2+\delta t} = \mathbf{R}_{\delta\theta}(\mathbf{q}^{t_1+\delta t}), \quad (1b)$$

where $\mathbf{q}^{t_n} = (\mathbf{u}^{t_n}, p^{t_n})$ refers to the system state variables (e.g., velocity and pressure) at time step t_n , $\omega(t)$ is the angular velocity of the rigid body, and $\mathbf{R}_{\delta\theta}$ denotes the rotation of angle $\delta\theta$. If we rewrite $\mathbf{q}^{t_n+\delta t}$ as the prediction of the model F from input \mathbf{q}^{t_n} , then Eq. 1b can be rewritten as

$$F_{\delta t}(\mathbf{q}^{t_2}) = \mathbf{R}_{\delta\theta}(F_{\delta t}(\mathbf{q}^{t_1})), \quad (2)$$

which can be further combined with Eq. 1a to produce

$$F_{\delta t}(\mathbf{R}_{\delta\theta}(\mathbf{q}^{t_1})) = \mathbf{R}_{\delta\theta}(F_{\delta t}(\mathbf{q}^{t_1})). \quad (3)$$

We further replace the ground truth model $F_{\delta t}$ with its surrogate \hat{F} and drop unnecessary superscripts and subscripts to arrive at

$$\hat{F}(\mathbf{R}(\mathbf{q})) = \mathbf{R}(\hat{F}(\mathbf{q})) \quad (4)$$

that should be satisfied for the surrogate model \hat{F} for system state \mathbf{q} at any instant and any rotation \mathbf{R} around the axis of rotation of the rotating body.

For a CFD solver, this property is usually enforced or at least approximately enforced by the minimization of the residual of the Navier-Stokes equation in every time step. For a surrogate model \hat{F} that does not directly enforce such solution by minimizing the Navier-Stokes residual, this property has to be enforced through a special treatment of the surrogate model itself or transformation of the system states into scalarized features. Interested readers are referred to the recent review by Han et al. [32] on various approaches to achieve rotation equivariance. For the current system of concern, however, we notice that under a polar (2D) or cylindrical (3D) coordinate system, any rotation \mathbf{R} will not change the magnitude of the velocity components and the pressure value, which means that the desired rotation equivariance is automatically achieved. We therefore adopt such coordinate systems in this work.

2.3. Spatial and temporal discretization

With the system domain Ω_f and the coordinate system described in Sec. 2.1 and 2.2, we proceed to write the governing equation of the fluid system into an abstract dynamical form as

$$\frac{d\mathbf{q}}{dt} = \tilde{F}(\mathbf{q}), \quad (5)$$

with \tilde{F} being the governing model for the system. Applying forward Euler temporal discretization with a fixed time step gives

$$\mathbf{q}^{t_{n+1}} - \mathbf{q}^{t_n} = \delta\mathbf{q} = F(\mathbf{q}(t_n)), \quad (6)$$

where \mathbf{q} denotes the state variables of the system, \mathbf{q}^{t_n} refers to these state variables at time step t_n , and F is the state update function after temporal discretization. For a fluid system, the system state \mathbf{q} usually includes the velocity \mathbf{u} and the pressure p . We further discretize Eq. 6 spatially with a mesh that co-rotates with the rotating body as mentioned in Sec. 2.1, leading to

$$\mathbf{Q}^{t_{n+1}} - \mathbf{Q}^{t_n} = \delta\mathbf{Q} = \mathbf{F}(\mathbf{Q}^{t_n}), \quad (7)$$

where \mathbf{Q}^{t_n} is the matrix containing system state variables at time step t_n , and \mathbf{F} is the function to update the state variables over each time step.

As mentioned in the Introduction, one could easily convert a mesh to a graph. If one performs such conversion from a mesh to a hypergraph $\mathcal{G} = (\mathcal{V}, \mathcal{E}_{\square}, \mathcal{E}_v)$ containing the set of all nodes \mathcal{V} , the set of all elements \mathcal{E}_{\square} , as well as the set of all element-node edges \mathcal{E}_v (cf. Fig. 1b), then one could

also transform the system states \mathbf{Q} into a series of features and attach them to the hypergraph as feature vectors. We assume that such conversion at each time step t_n leads to node feature vector $\mathbf{v}_i^{t_n}$ for each node i , element feature vector $\mathbf{e}_\square^{t_n}$ for each element \square , as well as element-node edge feature vector $\mathbf{e}_{\square,i}^{t_n}$ for each element-node edge connecting node i and element \square . The discretized time stepping (Eq. 7) can then be rewritten as

$$\mathbf{v}_i^{t_{n+1}} - \mathbf{v}_i^{t_n}, \mathbf{e}_\square^{t_{n+1}} - \mathbf{e}_\square^{t_n}, \mathbf{e}_{\square,i}^{t_{n+1}} - \mathbf{e}_{\square,i}^{t_n} = \mathbf{G}(\mathbf{v}_i^{t_n}, \mathbf{e}_\square^{t_n}, \mathbf{e}_{\square,i}^{t_n}), \quad (8)$$

in which \mathbf{G} is a single or a set of functions that updates the hypergraph features over each time step. Assuming static node and element features (which is true for this work), we can simplify Eq. 8 as

$$\mathbf{e}_{\square,i}^{t_{n+1}} - \mathbf{e}_{\square,i}^{t_n} = \mathbf{G}(\mathbf{v}_i, \mathbf{e}_\square, \mathbf{e}_{\square,i}^{t_n}). \quad (9)$$

A hypergraph neural network model $\widehat{\mathbf{G}}$ can be constructed as the surrogate for \mathbf{G} in Eq. 9. We briefly cover the architecture of the network architecture used in this work in the subsequent Sec. 2.4.

2.4. Network architecture

We adopt the recently proposed finite element-inspired ϕ -GNN [17] in the current work. Operating on a hypergraph discussed in the previous Sec. 2.3, the network mimics the local stiffness matrix calculation process in the finite element method, offering state-of-the-art performance along with explainability. Following the encode-propagate-decode fashion, the network contains a series of hypergraph message-passing layers between the encoding functions at the start and a decoding function at the end. With input node feature vectors \mathbf{v}_i , element feature vectors \mathbf{e}_\square , and element-node edge feature vectors $\mathbf{e}_{\square,i}$, different encoding functions g^v , g^e , and g^{ev} are applied to respective feature vectors:

$$\mathbf{v}_i \leftarrow g^v(\mathbf{v}_i), \quad (10a)$$

$$\mathbf{e}_\square \leftarrow g^e(\mathbf{e}_\square), \quad (10b)$$

$$\mathbf{e}_{\square,i} \leftarrow g^{ev}(\mathbf{e}_{\square,i}). \quad (10c)$$

The left arrow \leftarrow denotes an update of the parameter on its left-hand side by the value on its right-hand side. Each of the subsequent message-passing layers $\widehat{\mathbf{G}}_m$ containing an element update stage and a node update stage illustrated in Fig. 1c and 1d respectively. Assuming a hypergraph converted from a 2D quadrilateral mesh, for each layer m , the two update stages can be written as

$$\mathbf{e}_\square \leftarrow \text{AGG}_r^e(\varphi_m^e(\mathbf{v}_r, \mathbf{e}_\square, \mathbf{e}_{\square,r})), \quad (11a)$$

and

$$\mathbf{v}_i \leftarrow \text{AGG}_\square^v(\varphi_m^v(\mathbf{v}_i, \mathbf{e}'_{\square,i}, \mathbf{e}_{\square,i})) \quad (11b)$$

respectively, in which φ_m^e and φ_m^v are the element and node feature update function respectively, AGG denotes the mean aggregation function, $r = i, j, k, l$ denotes the index of the four nodes connected by the element, \square_i denotes any element that connects node i with other nodes, and $\mathbf{e}'_{\square,i}$ denotes the element feature vector after the element update stage (Eq. 11a).

In this formulation, we only need output on the element-node edges, and therefore only an element-node decoder is needed

$$\mathbf{e}_{\square,i} \leftarrow h^{ev}(\mathbf{v}_i, \mathbf{e}_\square, \mathbf{e}_{\square,i}). \quad (12)$$

that generates output element-node feature vector $\mathbf{e}_{\square,i}$ used in the time stepping of the flow field predictions, discussed later in Sec. 2.7.

Multi-layer perceptron. All the functions embedded within the graph neural network, including the encoding functions g^v , g^e , and g^{ev} , element update functions φ_m^e , node update functions φ_m^v , and the decoding function h^{ev} , are chosen as multi-layer perceptrons with two hidden layers in this work, which can be explicitly written as a function f to the input vector z

$$f(z) = \mathbf{W}_3 \sigma_2(\mathbf{W}_2 \sigma_1(\mathbf{W}_1 z + \mathbf{b}_1) + \mathbf{b}_2) + \mathbf{b}_3 \quad (13)$$

with weight matrices \mathbf{W}_i and bias vectors \mathbf{b}_i trainable for $i = 1, 2, 3$. The number of rows in the weight matrix \mathbf{W}_i is defined as the layer width, and the nonlinear function σ_i is usually called the activation function.

2.5. Local directed pressure difference

In existing works, when the pressure is modeled in a surrogate model for a flow system, it is usually used directly as a feature to be predicted over time. This practice implicitly assumes that there is a Dirichlet pressure boundary in the domain. However, when such a pressure boundary does not exist, however, the pressure value everywhere in the domain is essentially undefined, since only the spatial gradient of the pressure is involved in the Navier-Stokes equation rather than the pressure itself. In CFD simulations one usually resolves such an issue by designating a pressure reference point which acts as an artificial Dirichlet pressure boundary condition. With a surrogate model, we observe during the preliminary tests that such practice can inhibit the convergence of the training process. To resolve this issue, we propose to model the local pressure gradients rather than the pressure itself. In particular, with the mesh and hypergraph defined in Fig. 1b, for any element, one could approximate the pressure gradient in the direction pointing from element \square to node d via

$$\nabla_{\mathbf{x}_{\square,d}} p \approx \frac{p_d - \overline{p_d}}{L_{\square,d}} \quad (14)$$

with first-order accuracy, where d denotes any node connected by the element \square , the overline $\overline{(\cdot)}$ denotes averaging over all nodes within the element, and $\mathbf{x}_{\square,d}$ denotes the direction of the element-node edge pointing from the node d to the element center. In practice, under the limitation of numerical stability, we do not directly model this approximated local pressure gradient but rather model only its numerator, i.e., the change of pressure $\delta p_{\square,d} = (\nabla_{\mathbf{x}_{\square,d}} p) L_{\square,d} = p_d - \overline{p_d}$ from the center of element \square to node d . We coin such pressure increment value *local directed pressure difference*.

2.6. Geometry features, graph feature attachment

Apart from the flow information, i.e., the velocity and pressure, we also transform the geometry information, specifically the mesh coordinates and the neighborhood information into features. Given an element \square connecting within a polar coordinate system on 2D, we encode the radius r as well as the boundary condition γ on the nodes, leading to node feature vector

$$\mathbf{v}_d = [r_d \quad \gamma_d]^T. \quad (15)$$

where d denotes each of the nodes connected by the element. In both of test cases that will be reported in Sec. 4 there is only one boundary condition (which is the fluid-solid interface), which means that the boundary condition γ_d is set to [1] if the node d is on the interface and [0] otherwise. The element feature vector contains only the radius r_{\square} of the element center, and we augment this vector by its negative value to avoid a vector length of 1,

$$\mathbf{e}_{\square} = [r_{\square} \quad -r_{\square}]^T. \quad (16)$$

The information on the relative location between the nodes connected by the element is encoded in the element-node features. For a 2D case within a polar coordinate system, we calculate the relative polar radius and angle of each node d from the element \square ,

$$\begin{aligned} r_{\square,d} &= r_d - r_{\square} \\ \theta_{\square,d} &= \theta_d - \theta_{\square} \end{aligned} \quad (17)$$

where r_d and θ_d are the polar radius and polar angle of each node d , and r_{\square} and θ_{\square} are the polar radius and polar angle of the element geometric center. For a 3D case within a cylindrical coordinate system, we additionally calculate the relative coordinate in the z direction,

$$z_{\square,d} = z_d - z_{\square} \quad (18)$$

By the aforementioned transformation of the coordinates and connectivity we ensure that the information is sufficient to fully define the shape of the element, whilst also enforces invariance to translation in z direction and rotation around the z axis, which are necessary for enforcing translation invariance and rotation equivariance of the prediction from the GNN framework. We assemble the transformed element-node geometry features with the velocity and pressure information, leading to the element-node feature vectors for 2D cases

$$\mathbf{e}_{\square,i} = [u_{r,\square,d} \quad u_{\theta,\square,d} \quad \delta p_{\square,d} \quad r_{\square,d} \quad \theta_{\square,d} \quad Re]^T \quad (19a)$$

where the element-node velocity features are gathered from the nodes to their connected element-node edges:

$$\begin{aligned} u_{r,\square,d} &\leftarrow u_{r,d} \\ u_{\theta,\square,d} &\leftarrow u_{\theta,d} \\ u_{z,\square,d} &\leftarrow u_{z,d} \end{aligned} \quad (19b)$$

This is a design choice that serves to prevent the generation of more than one term in the loss and therefore avoid the need for weight factors between different loss terms. We attach the Reynolds number as an additional feature since the 2D test case presented later in Sec. 3 and 4 span a range of Reynolds numbers. As the 3D case presented in this work only contains flow data at a single Reynolds number, we can skip such feature and the element-node feature vector is thus

$$\mathbf{e}_{\square,i} = [u_{r,\square,d} \quad u_{\theta,\square,d} \quad u_{z,\square,d} \quad \delta p_{\square,d} \quad r_{\square,d} \quad \theta_{\square,d} \quad z_{\square,d}]^T \quad (19c)$$

2.7. Time stepping and post-processing

As discussed in Sec. 2.3, the network is constructed as a surrogate model for the ground truth feature update function \mathbf{G} in Eq. 9. Specifically, the gathered velocity and the local directed pressure difference values on the element-node edge feature vectors are iteratively predicted by the graph neural network

$$\begin{aligned} \mathbf{e}_{\square,i}^{t_n+1} &= \mathbf{e}_{\square,i}^{t_n} + \begin{bmatrix} \mathbf{u}_{\square,i}^{t_n+1} - \mathbf{u}_{\square,i}^{t_n} \\ \delta p_{\square,i}^{t_n+1} - \delta p_{\square,i}^{t_n} \\ \mathbf{0}_{2 \times 1} \end{bmatrix} \\ &\approx \mathbf{e}_{\square,i}^{t_n} + \begin{bmatrix} \widehat{\mathbf{G}}(\mathbf{v}_i, \mathbf{e}_{\square}, \mathbf{e}_{\square,i}^{t_n}) \\ \mathbf{0}_{2 \times 1} \end{bmatrix} \end{aligned} \quad (20)$$

with $\mathbf{u}_{\square,i} = [u_{r,\square,i} \quad u_{\theta,\square,i}]^T$ for 2D cases and $\mathbf{u}_{\square,i} = [u_{r,\square,i} \quad u_{\theta,\square,i} \quad u_{z,\square,i}]^T$ for 3D cases. The predicted values at each time step are then post-processed to retrieve the predicted system states on each node. For the velocity terms, the value at each node is obtained by evaluating the mean across all element-node edges connecting the node with any element

$$\hat{u}_{r,i}^n = \text{MEAN}_{\square}(\hat{u}_{r,\square,i}^n), \quad (21a)$$

$$\hat{u}_{\theta,i}^n = \text{MEAN}_{\square}(\hat{u}_{\theta,\square,i}^n), \quad (21b)$$

in which MEAN_{\square} is the mean aggregation function. When local pressure is needed instead of the local pressure gradient, such as during the calculation of the force on the solid body, one could recover the pressure value on the nodes in the post-processing steps through an approach similar to that of CFD: designate a single element as the pressure reference and then solve a linear system to obtain the pressure values on all or a part of the nodes, laid out in Algorithm 1. For cases where the connectivity of the hypergraph \mathcal{G} stays unchanged over time, the pseudoinverse A^{\dagger} can be re-used, reducing the computational overhead of this post-processing step to a matrix-vector product.

Algorithm 1 Procedure to recover nodal pressure values from local directed pressure differences

Input: Hypergraph $\mathcal{G} = (\mathcal{V}, \mathcal{E}_{\square}, \mathcal{E}_v)$, with number of nodes n_v , number of elements n_e , number of nodes connected by each element n_{ev} , connectivity matrix $\mathbf{C} \in \mathbb{N}^{n_e \times n_{ev}}$, and local pressure difference $\delta \mathbf{p}_{\square,i} \in \mathbb{R}^{n_e \times n_{ev}}$ attached to element-node edges.

Initialize $\mathbf{A} = \mathbf{0}_{(n_e n_{ev} + 1) \times n_v}$

for $i = 1 : n_e$ **do**

$\square_i = \mathbf{C}[i, 1 : n_{ev}]$

$\mathbf{A}[(i-1)n_{ev} : (in_{ev}-1), \square_i] = \frac{n_{ev}-1}{n_{ev}} \mathbf{I}_{n_{ev} \times n_{ev}} - \mathbf{1}_{n_{ev} \times n_{ev}}$

end for

$\mathbf{A}[n_e n_{ev}, \square_i] = \mathbf{I}_{1 \times n_{ev}}$

Flatten $\delta \mathbf{p}_{\square,i}$ to an $\mathbb{R}^{n_e n_{ev} \times 1}$ vector in row-major order

$p_i = \mathbf{A}^{\dagger} \delta \mathbf{p}_{\square,i}$

Output: Nodal pressure value p_i

3. Experimental setup

With the framework constructed in Sec. 2, we proceed to apply this framework to cases featuring fluid flow around rotating structures. For this purpose, we consider two test cases. The setup of these cases will be discussed in the subsequent Sec. 3.1, including the CFD setup and also how the training and test data sets are obtained. After that, we describe the implementation of the network and its training details in Sec. 3.2 to Sec. 3.4. We finally list the metrics that will be used to compare between the GNN predictions and the ground truth CFD results in Sec. 3.5.

3.1. Setup of the test cases

We test our proposed framework on two test cases, one in 2D and the other in 3D. The 2D test case features a set of three cylinders that form a line and rotate around the center of the middle cylinder, which is similar to the cross section of a stirring mixer in a sealed container. The 3D test case involves the flow around a rotating cube, which is one of the simplest 3D scenarios that both involves flow around rotating structures and cannot be modeled via axis-symmetric 2D simulation. In the remainder of this subsection, we will describe how the simulation is performed, how the flow data are sampled, and how these flow data are pre-processed to obtain the training and test data sets for the two test cases.

Solver setup. We use open-source package openFOAM [33] to generate ground-truth CFD data for both test cases. The Navier-Stokes equations are discretized using the finite-volume method. The time derivatives are discretized by a second-order implicit scheme, and the divergence, gradients, and diffusion terms are discretized via a second-order Gaussian integration scheme. The discretized equations are solved by the Pressure-Implicit with Splitting of Operators (PISO) algorithm [34] with one non-orthogonal corrector. The tolerance for both velocity and pressure residuals are set to be 1×10^{-6} . We validate the numerical scheme by running the 3D test case (described later in this subsection) without

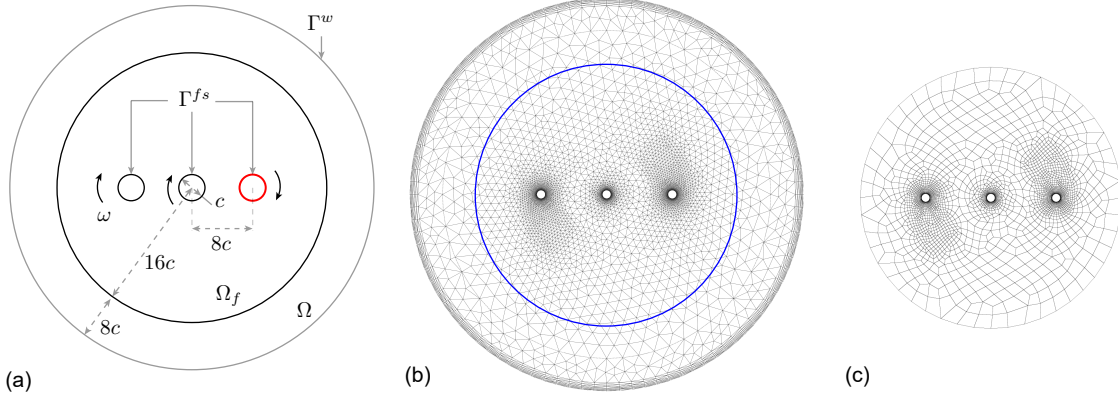


Figure 2: (a) Schematic of the computational domain for the 2D test case, (b) mesh used for the CFD simulation, with the blue circle marking out the boundary of Ω_f , and (c) mesh used by the GNN surrogate model. Lift and drag coefficients will be calculated for the cylinder marked by red in (a).

cube rotation. The average drag coefficient is calculated to be $c_d = 0.935$ in this validation case, which is between the values obtained from empirical formulas by Hölzer et al. [35] ($c_d = 0.854$) and Haider and Levenspiel [36] ($c_d = 1.122$). We therefore believe that the simulation results are reasonable.

2D case: flow around a rotating mixer. A schematic of the simulation domain for the 2D test case is shown in Fig. 2a. One cylinder of diameter c sits on the origin, while two other cylinders are located with a distance $L_c = 8c$ from this central cylinder. All three cylinders rotate around the center of the central cylinder at a fixed angular velocity ω . The fluid domain Ω_f is bounded by a circular outer wall at $R_w = 24c$. The no-slip boundary condition is applied to the cylinder surface Γ^{fs} and the outer wall Γ^w . This setup is similar to a cross section of a mixer inserted in a sealed can, and also similar to the cross section of a vertical axis wind turbine if one changes the two outer cylinders to airfoils and replaces the outer wall with a background uniform flow.

With the mesh shown in Fig. 2b, we generate a series of simulations at Reynolds numbers $Re = U_c c / \nu = 130, 133, 137, 140, 143, 147, \dots, 230$ that are used to train and cross-validate the model, and a series of simulations at Reynolds numbers $Re = 135, 145, 155 \dots, 225$ that are used to test the model, where $U_c = \omega L_c$ is the center velocity of the two off-origin cylinders. All these simulations are performed with the Courant number limit $Co \leq 0.9$. We sample the train and test data sets at each Reynolds number after the simulation reaches the statistically stationary state, with the non-dimensionalized sampling time step $\Delta t^* = \Delta t U_c / c = 0.32$. Every sampling time step is equivalent to the size of around 5 to 6 CFD time steps (which varies for different Reynolds numbers). For each train/cross-validate Reynolds number, we sample 2049 continuous time steps. For each test Reynolds number, we sample 2001 continuous-time steps. The flow data samples are loaded via the fluidFOAM package [37] and subsequently interpolated onto the mesh drawn in Fig. 2c using a clough-tocher 2D interpolation available in the SciPy package [38]. The interpolated flow data are then processed into training, cross-validation, and test data sets, described later in this subsection.

3D case: flow around a rotating cube. A schematic of the domain Ω for the 3D test case is shown in Fig. 3a. A right cube (i.e., a regular hexahedron) is placed with its center at the origin, and its six faces facing $\pm x, \pm y, \pm z$ directions respectively at $t^* = 0$. The cube rotates around $+z$ -axis with advance ratio $J = 2U_\infty / (\omega c) = 0.952$, where U_∞ is the inlet flow velocity, ω is the angular velocity, c is the border length of the cube. The simulation domain is defined as a cylinder that contains the cube. A uniform flow enters the domain at the inlet Γ^{in} with the flow in the $-z$ direction. The outlet Γ^{out} is a mixed boundary condition with the total pressure set to zero, the outlet velocity gradient set to zero,

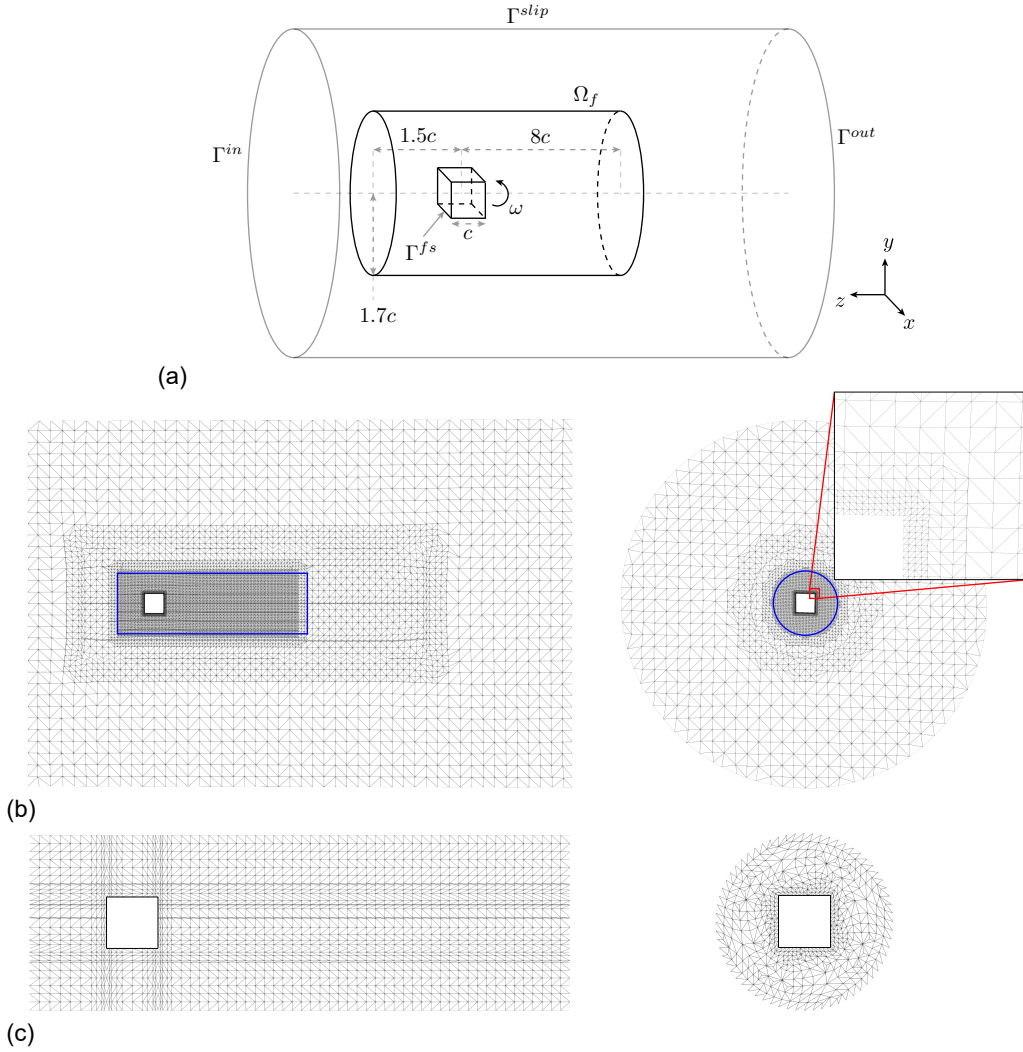


Figure 3: (a) Schematic of the computational domain for the 3D test case, (b) mesh used for the CFD simulation, with the blue rectangle and circle marking out the boundary of Ω_f , and (c) mesh equivalent to that used by the GNN surrogate model. Note that the actual mesh used in the GNN is recombined to semi-structured hexahedrals from the mesh plotted in (c).

and the inlet velocity based on the flux in the z direction. No slip boundary condition is assigned to the surface Γ^{fs} of the cube, and the slip boundary condition is assigned to the remaining boundaries Γ^{slip} of the domain. With the mesh plotted in Fig. 3b, we generate simulation data at Reynolds number $Re = 500$ with a non-dimensionalized time step $\delta t^* = \delta t U_\infty / c = 3 \times 10^{-3}$, which corresponds to Courant number $Co \approx 0.64$. After the simulation reaches stationary state, we sample 2561 continuous time steps at interval $\Delta t^* = 3 \times 10^{-2}$ (i.e., every 10 CFD time steps) that are then processed into training and cross-validation data set, and another (without overlapping with the training set) 2001 continuous time steps at the same interval for test data set. The sampled and loaded flow data are interpolated onto the mesh drawn in Fig. 3c using a linear barycentric interpolation. The interpolated flow data are then processed into training, cross-validation and test data sets.

Construction of training, cross-validation, and test data sets. With the flow data sampled, we proceed to construct the data sets. We construct the training samples following Eq. 20, meaning that the 2049 continuous time steps sampled for each of the training Reynolds numbers in the 2D test case can be

Table 1: Various statistics for the test cases. The peak GPU memory overhead occurs during training, memory overhead during inference is very low.

Case	Type	Mesh size (number of cells/elements)	Cores/Partitions	Train speed (sec/epoch)	Peak GPU Memory (GB)	Inference speed (ms/GNN step)
2D	CFD	9358 (pure tri)	2	-	-	580 (116×5)
	GNN	3313 (pure quad)	1	1977	5.9	35.1
3D	CFD	385883 (mostly hex)	12	-	-	8310 (831×10)
	GNN	39507 (pure hex)	1	1101	19.1	149
			2	1404	13.8	
			3	1723	12.8	
			5	2390	10.4	
10	3911	9.1				

separated into 2048 training samples, with each sample containing input-output pair

$$\begin{aligned}
 \text{Input: } & \mathbf{v}_i, \mathbf{e}_{\square}, \mathbf{e}_{\square,i}^{t_n} \\
 \text{Output: } & \begin{bmatrix} \mathbf{u}_{\square,i}^{t_n+1} - \mathbf{u}_{\square,i}^{t_n} \\ \delta p_{\square,i}^{t_n+1} - \delta p_{\square,i}^{t_n} \end{bmatrix}
 \end{aligned} \tag{22}$$

for time step $n = 1, 2, \dots, 2048$. The training samples from all training Reynolds numbers are then concatenated to form the training set. The 2561 continuous-time steps sampled in the 3D test case are separated into a training data set with 2560 training samples likewise. The input node features, element features, element-node edge features, and output element-node edge features are then normalized via min-max normalization with minimum -1 and maximum 1 , respectively, for each test case. For cross-validation and test data sets, we construct the input to the neural network using the first time step of the sampled data in the same way as we construct the training input and then normalize such input using the normalization statistics (i.e., the scaling and shift factors) calculated from the training data set.

3.2. Network setup and training

The networks are implemented via PyTorch [39]. A ϕ -GNN with 15 layers is used to model the 2D rotating mixer case, and another ϕ -GNN with 10 layers is used for the 3D rotating cube case. For both networks, the encoding, decoding, node and element update functions are all selected as multi-layer perceptrons with two hidden layers of width 192, activated by sinusoidal activation function [40]. All aggregation functions are chosen as the mean function.

Hardware settings. All training and tests are performed with a single Nvidia RTX 3090 GPU with CPU being AMD Ryzen 9 5900 @ 3.00 GHz×12 cores. We cap the CPU frequency at 2.91 GHz to avoid performance fluctuations. The GPU is downclocked by 593 MHz and limited to 75% power during training for the same reason, but unlimited during evaluation since the bottleneck for prediction roll-out speed is CPU power. The test runs are performed without these limitations. We report the training and inference speed along with the GPU memory overhead in Table 1.

Training scheme & loss. An Adam [41] optimizer with $\beta_1 = 0.9$ and $\beta_2 = 0.999$ is used for the training. The network is trained for 50 epochs for the 2D case and 200 epochs for the 3D case. In both cases, the learning rate is adjusted at the start of every epoch following a merged cosine-exponential scheme [17] with maximum learning rate 8×10^{-5} and minimum learning rate 1×10^{-6} . It should be noted that the maximum learning rate adopted in this work is set to be slightly lower than the value (1×10^{-4}) in earlier works [17] due to the use of mixed precision training (cf. Sec. 3.3). For the 3D case, a warmup stage of 10 epochs is employed at the start of training, where the learning rate is adjusted every training iteration from 1×10^{-5} to 8×10^{-5} following an adjustment scheme that is the reverse of the main training stage. An adaptive smooth L_1 loss [17] is used, which calculates the loss for ground truth ψ and its neural network prediction $\hat{\psi}$ as

$$L_i(\psi_i, \hat{\psi}_i) = \begin{cases} (\psi_i - \hat{\psi}_i)^2 / 2\beta, & \text{if } |\psi_i - \hat{\psi}_i| < \beta \\ |\psi_i - \hat{\psi}_i| - \beta/2, & \text{if } |\psi_i - \hat{\psi}_i| \geq \beta \end{cases} \quad (23)$$

where the subscript $(\cdot)_i$ denotes entry-by-entry calculation, and β controls the transition point between the L_2 loss region and the L_1 loss region, updated after each training iteration with

$$\beta^2 \leftarrow (1 - \frac{1}{N_b})\beta^2 + \frac{1}{N_b} \min\{\beta^2, \text{MSE}(\psi_{batch}, \hat{\psi}_{batch})\} \quad (24)$$

in which N_b is the total number of training iterations within each epoch, and MSE denotes the mean-squared loss. Since the β value is updated on-the-fly, its initial value only has a minor impact on the final results as long as such value is not set too close to zero, in which case the loss reduces to an L_1 loss. In this study, we manually set this value as 1×10^{-3} for the 2D case and 1×10^{-2} for the 3D case, close to the L_2 loss at the start of the training for the two cases.

Training noise. Assuming normally-distributed single-step prediction error at each time step, we adopt the training noise scheme from [17], with which we add a Gaussian noise of $(\kappa \odot \hat{\epsilon}_{\square,i}^n, -\omega \hat{\epsilon}_{\square,i}^n)$ to each input-output pair (i.e., each training sample), where κ is the vector containing the scaling factors used during the min-max normalization of training output targets. The over-correction factor is set to $\omega = 1.2$. Each entry of $\hat{\epsilon}_{\square,i}^n$ is randomly and individually sampled from a normal distribution, i.e.,

$$\hat{\epsilon}_{\square,i}^n \sim \mathcal{N}(0, \text{Var}(\hat{\epsilon}_{\square,i}^n)) \quad (25)$$

The variance of the noise adopted in this work are $\text{Var}(\hat{\epsilon}_{\square,i}^n) = 6.25 \times 10^{-4}$ for the 2D case and 2.5×10^{-3} for the 3D case. These choices are made by starting from 6.25×10^{-4} (which is the minimum variance used in [17]) and iteratively quadruple the variance until the network is able to generate stabilized predictions on the cross-validation set.

3.3. Mixed precision training

To reduce memory overhead and improve inference speed, models are trained through mixed precision training, with which almost all calculations are performed with the floating point number of half precision (fp16) rather than the typical floating point number of a single precision (fp32). Since half-precision floating point numbers offer significantly lower precision compared with single precision ones, to prevent gradient underflow, we followed the standard practice [42] to scale up the loss by a multiplier λ during the gradient calculation process, and the calculated gradients are scaled back afterwards. In this work, this multiplier starts with $\lambda = 2^{11} = 2048$, and doubles its value when $\lambda\beta < 125$ is satisfied at the start of any epoch, where β is the parameter updated on-the-fly in Eq. 24. The constant 125 is obtained from preliminary tests to ensure that the loss and the gradient do not overflow (i.e., the absolute value of their magnitude stays within 65504, the upper limit of half-precision floating point numbers) for ϕ -GNNs. Since the smallest positive number that can be expressed with half-precision floating point number is around 6×10^{-8} , we also adjust the ϵ value in the denominators within the optimizer to 10^{-6} for the 2D case and 10^{-7} for the 3D case rather than the default 10^{-8} to improve numerical stability.

3.4. Gradient accumulation from graph partitions

For certain cases, especially in 3D scenarios, the hypergraph converted from the mesh can be too large such that the model cannot be trained on a single GPU unit with batch size 1. In order to reduce the memory overhead during the training process and make it possible to train cases with a larger mesh size, we partition the hypergraph into multiple segments, calculate the gradients using each segment sequentially, and recover the gradient for the whole sample by accumulating the gradients calculated from all the segments.

To ensure that the gradients calculated from the entire hypergraph and that accumulated from the segments match within machine precision, the construction of a *buffer region* around each segment is necessary. To illustrate such a construction process, we consider a simple hypergraph converted from a mesh drawn in Fig. 4. The hypergraph of a single training sample is first partitioned into multiple segments by some criteria, and we mark out one of these partitions, partition A, with the red color in Fig. 4a. In the second step, we start from each segment and mark out the 'buffer' region by first marking all the elements within the segment with an element feature vector $e_{\square} = [\text{True}]$ and all elements out of the segment with an element feature vector $e_{\square} = [\text{False}]$, and then iterate over the following hypergraph message-passing layers that serves to expand the marked region:

$$\mathbf{v}_i \leftarrow \text{OR}_{\square}^v(e_{\square_i}), \quad (26a)$$

$$e_{\square} \leftarrow \text{OR}_r^e(\mathbf{v}_r), \quad (26b)$$

where e_{\square_i} in Eq. 26b denotes the element feature vector of each element connecting node i to some other nodes, \mathbf{v}_r in Eq. 26a denotes the node feature of each node connected by the element \square , and OR denotes logical or aggregation. Each execution of Eq. 26 extends the buffer region by one hop. This process is repeated the same number of times as the designed layer depth of the hypergraph neural network, and after that Eq. 26a is executed one last time.

We show such an iterative process with a layer depth of two in Fig. 4b-4e. Each segment is then separated along with its buffer region from the hypergraph using the calculated mask \mathbf{v}_i for nodes and e_{\square} for elements and element-node edges, illustrated in Fig. 4f. Each separated segment is then renumbered in the third step and then sent into the forward pass of the training like an individual sample. During the loss calculation, the buffer region is discarded (i.e., only the loss on the element-node edges marked by the red color will be calculated). Eventually, the gradients calculated from all segments of each training sample are accumulated through a weighted average to recover the true gradients corresponding to the training sample. The final gradients obtained from this weighted average are the same as the gradients calculated with the whole training sample (i.e., batch size 1), and are used to update the parameters of the network.

In implementation, we replace the logical values of True and False by 1 and 0 respectively, and the aggregation in Eq. 26 will be changed to max aggregation as a result. The buffers of all segments are also calculated in parallel by constructing a $n_s \times 1$ initial element feature vector, where n_s is equal to the number of segments, such that the i -th entry of the feature vector of each element denotes whether the element belongs to the i -th segment. The aforementioned buffer construction process can then be applied to obtain the masks for all segments together. We apply this partitioning and buffer construction approach to the 3D test case used in this work. Since the mesh is structured in the z direction, we simply partition the mesh by multiple planes parallel to the $x - y$ plane, such that each partition covers the same length in the z direction. We report the peak memory cost during training for different number of partitions in Table 1.

Remark 1. *It should be noted that Dupuy et al. [30] directly use each graph fragment as a single training sample instead of accumulating the gradients. However, we notice that different fragments could vary significantly in physics, leading to possible instability in the training process. We therefore choose to accumulate the gradients calculated over all the mesh fragments to recover the true gradient for the whole hypergraph before updating the parameters within each training iteration.*

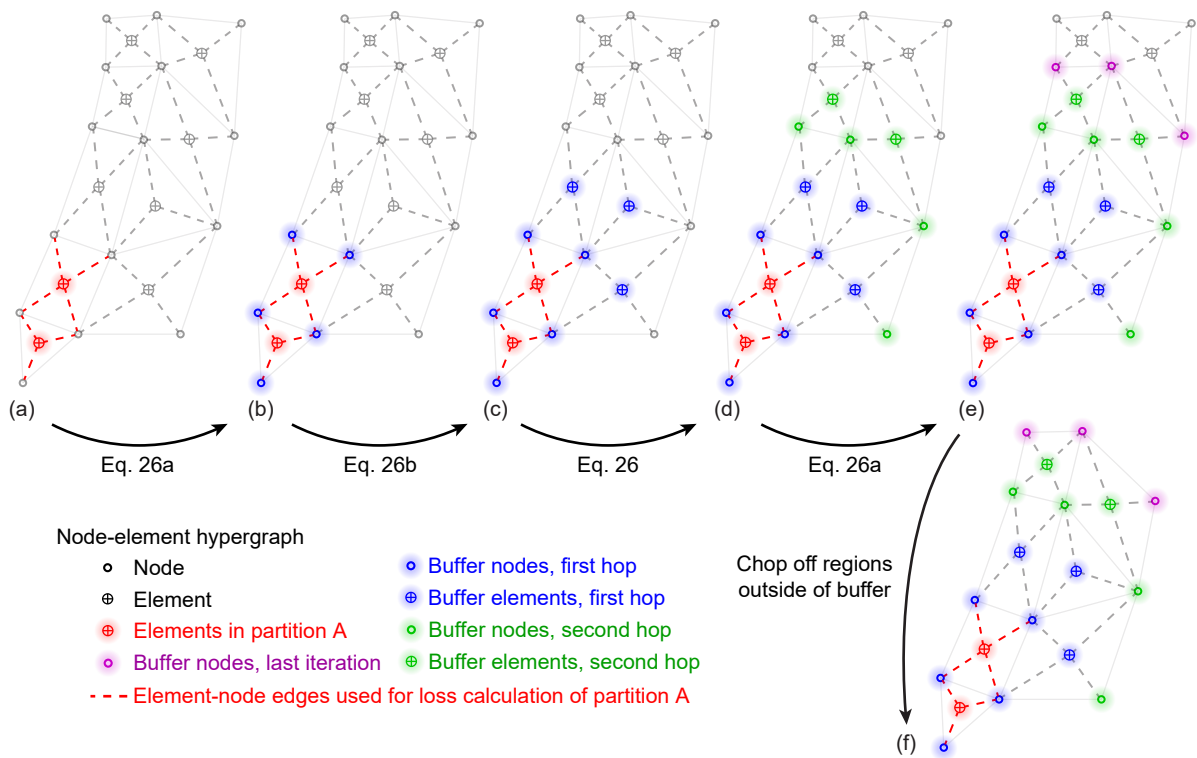


Figure 4: Construction of the buffer region for each partition. (a) The partition A of a mesh, (b) the buffer nodes are identified in the first hop, (c) the buffer elements are identified in the first hop, (d) The buffer nodes and elements are identified in the second hop, (e) The buffer nodes are identified in the last iteration, and (f) The partition and its buffer region are separated from the remaining parts of the hypergraph.

3.5. Evaluation metrics

We test the trained networks in the test data sets to evaluate their performance. Similarly to existing work such as [13, 17], we use both qualitative and quantitative metrics to facilitate evaluation. For the qualitative measure, we compare the velocity magnitude fields obtained from the predictions versus those from CFD simulations (i.e., the ground truth data). For the 2D test case, we will plot the whole field. For the 3D test case, several 2D slices of the predicted field will be extracted for comparison.

In this work, we employ a few quantitative measures. To compare the similarity between the whole predicted fields, we employ the coefficient of determination R^2 , defined as

$$R^2 = 1 - \frac{\|\mathbf{q} - \hat{\mathbf{q}}\|_2^2}{\|\mathbf{q} - \bar{\mathbf{q}}\|_2^2}, \quad (27)$$

for any system state \mathbf{q} and its prediction $\hat{\mathbf{q}}$. A coefficient of determination close to 1 indicates close matching between the predicted and ground-truth system states. We additionally extract the forces on the solid body from the predicted system states and compare those with the forces calculated from the ground-truth values. This calculation is achieved by integrating the Cauchy stress tensor $\boldsymbol{\sigma}^f = -p^f \mathbf{I} + \mu^f (\nabla \mathbf{u}^f + (\nabla \mathbf{u}^f)^T)$ on the surface of the solid body Γ_{fs} using the first layer of elements of that surface. For the 2D test case, we calculate the drag (in the direction of θ -axis), and also the lift (in the direction of the r -axis) via

$$C_r = \frac{1}{\frac{1}{2}\rho^f (U_c)^2 c} \int_{\Gamma_{fs}} (\boldsymbol{\sigma}^f \cdot \mathbf{n}) \cdot \mathbf{n}_r d\Gamma, \quad (28a)$$

$$C_\theta = \frac{1}{\frac{1}{2}\rho^f (U_c)^2 c} \int_{\Gamma_{fs}} (\boldsymbol{\sigma}^f \cdot \mathbf{n}) \cdot \mathbf{n}_\theta d\Gamma. \quad (28b)$$

where c is the diameter of the cylinder. We implement these calculations by calculating the forces in the x and y directions in Cartesian coordinates and then projecting them in the time-dependent r and θ direction at every time step. For the 3D test case, due to the rotation motion, we only calculate the drag force

$$C_d = \frac{1}{\frac{1}{2}\rho^f (U_\infty)^2 c^2} \int_{\Gamma_{fs}} (\boldsymbol{\sigma}^f \cdot \mathbf{n}) \cdot \mathbf{n}_z d\Gamma, \quad (29)$$

where c is the border length of the cube.

4. Results and discussion

4.1. Experiment – flow in a 2D mixer

The network was trained following the setup discussed in Sec. 3 is tested on a series of test flow data sets obtained in Reynolds numbers $Re = 135, 145, 155 \dots, 225$, evenly distributed within the training Reynolds number range. At each of the testing Reynolds numbers, we start from the first step within the test data set, and generate roll-out predictions of the system states (velocity and pressure) over the following 2000 time steps. Stabilized predictions are obtained for all test data sets. We present these results in the remainder of this subsection. We notice that the Reynolds number range for training and test $Re \in [130, 230]$ covers both the periodic and chaotic flow regimes, with the transition occurring around $Re = 180$. We therefore report the results in three among all the test datasets, which corresponds to the periodic, transition, and chaotic regime, respectively.

Prediction for periodic flow. Similar to existing applications of ϕ -GNN, we observe that the network is able to make accurate predictions over the entire 2000 prediction time steps when the flow system is in the periodic regime. As an example of the results within this regime, we report the GNN predictions and compare them with the CFD results for the test data set at $Re = 135$. The coefficient of determination R^2 value over the prediction time steps, plotted in Fig. 5a, stays at a value close to 1, indicating a close match between the predictions made by GNN and the CFD results. One may notice that the R^2 exhibits greater and greater fluctuation over the prediction time steps. This is largely due to the phase error accumulated during the prediction rollout, which eventually leads to a minor phase shift after thousands of time steps. We report the lift and drag on one of the two outer cylinders in Fig. 5b, and a minor phase shift of the lift and drag forces calculated from the predicted system states can also be observed near the end of the prediction roll-out. We additionally report the predicted versus the ground truth velocity magnitude field at prediction steps 1934, 1967, and 2000 in Fig. 5c for visual comparison.

Predictions in the transition regime. The flow system gradually becomes chaotic at around $Re = 180$. We report the results for the test data set at $Re = 185$, which demonstrates weakly chaotic behavior. The coefficients of determination, as well as the lift and drag coefficients, plotted in Fig. 6a-6b, show that the network is able to generate stabilized and accurate predictions for such weakly chaotic flow system over the entire 2000 time steps. We again plot the predicted versus ground-truth velocity magnitude field at prediction steps 1934, 1967, and 2000 in Fig. 6c.

Predictions for chaotic flow. With increasing Reynolds numbers the system eventually becomes chaotic. For this chaotic regime, we report the results from the test data set at Reynolds number $Re = 225$. Whilst the network is still able to make stabilized predictions, these predictions start to deviate significantly from the CFD results and are no longer accurate after a few hundred time steps. In the meantime, we notice that the predictions of the first 500 time steps are quite accurate for such a chaotic system, regardless of the prediction starting point, as demonstrated in Fig. 7a-7b. The flow field predictions are also accurate for the first 500 time steps, as plotted in Fig. 8.

4.2. Experiment – flow around a rotating cube

System state predictions, accumulated phase error. For the 3D test case, we plot the coefficient of determination for the velocity magnitude $|U|$ and local pressure difference $p_{\square,i}$ in Fig. 9a, with the predicted versus ground truth velocity magnitude fields in sampling planes $x = 0$, $z = 0$, and $z = -5c$ plotted in Fig. 9d. The R^2 value is stable over the prediction rollout, but decays significantly to around 0.88 at rollout time step 2000. We notice, however, that such decay is also caused a minor phase shift accumulated during the prediction rollout, similar (but more significant in the accumulated amount) to that of the $Re = 135$ test set in the 2D test case. To demonstrate this phase shift, we plot the R^2 value between prediction time step 2000 and different ground truth time steps from 1981 to 2000 in Fig. 9b, and one could notice that the predicted flow field at time step 2000 is the most similar to the CFD results at time step 1992 with $R^2 = 0.9996$, showing a predominant phase error equivalent to about 8 time steps. This error is also visible from the flow fields sampled, as marked out by the red rectangles and the magenta circles in Fig. 9d.

Drag force predictions. We plot the predicted versus ground truth drag coefficients in Fig. 9c. We observed that the mean force coefficients calculated from the graph neural network predictions are close to those of the CFD results. In addition, we observe that the instantaneous drag coefficients from the GNN predictions are close to the moving average of the instantaneous force coefficients calculated from the CFD results. As the drag force is directly calculated from the predicted flow fields, this observation shows that the graph neural network is able to automatically filter out high frequency fluctuations when learning the large-scale spatio-temporal evolution of the fluid system.

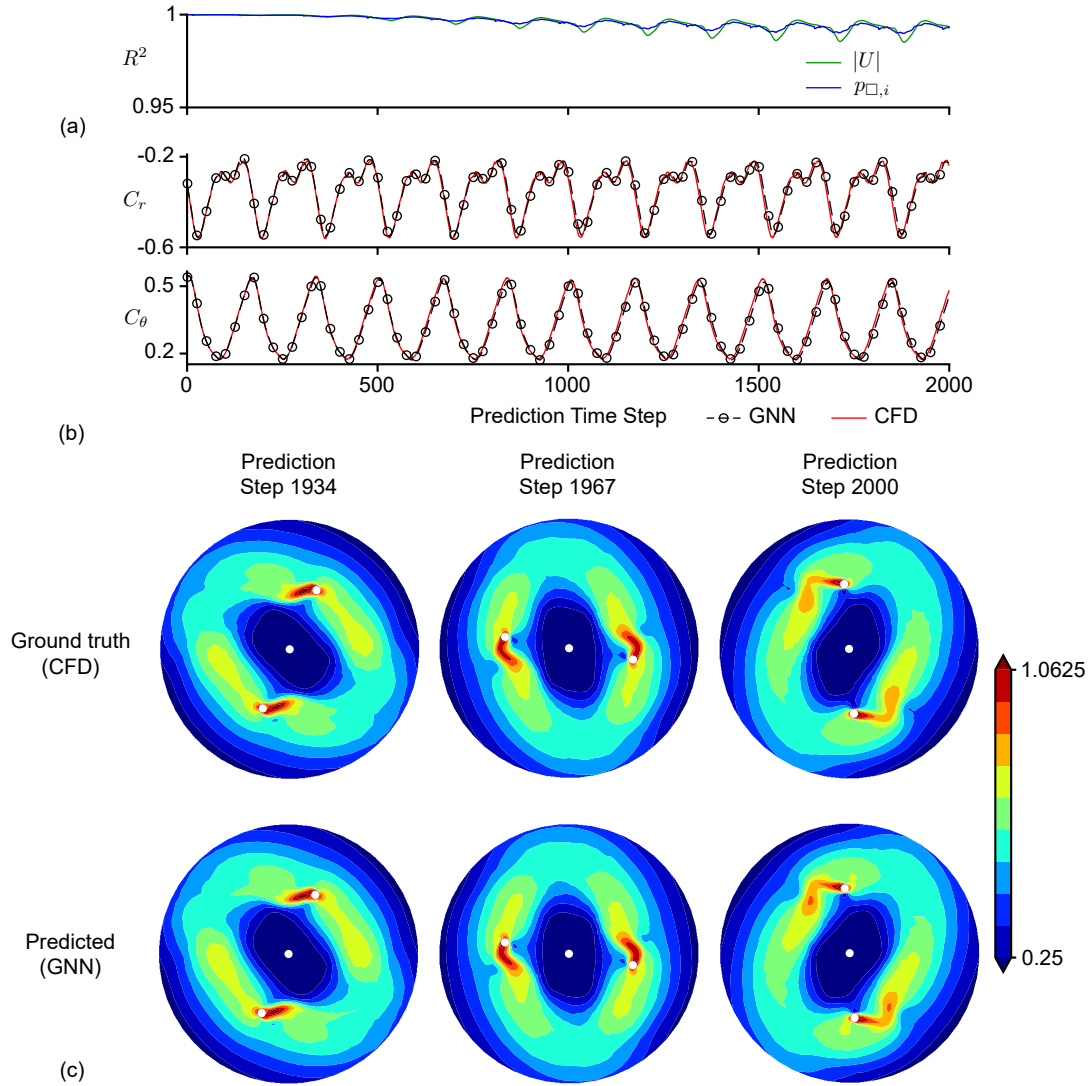


Figure 5: Results for the 2D test data set at $Re = 135$, featuring periodic flow behavior. (a) Coefficient of determination between ground truth and predicted flow fields at every prediction time step, (b) lift and drag coefficients calculated from the ground truth and predicted flow fields for the cylinder marked in red in Fig. 2a at every prediction time step, (c) normalized velocity magnitude $|U|^*$ field at prediction time steps 1934, 1967, and 2000.

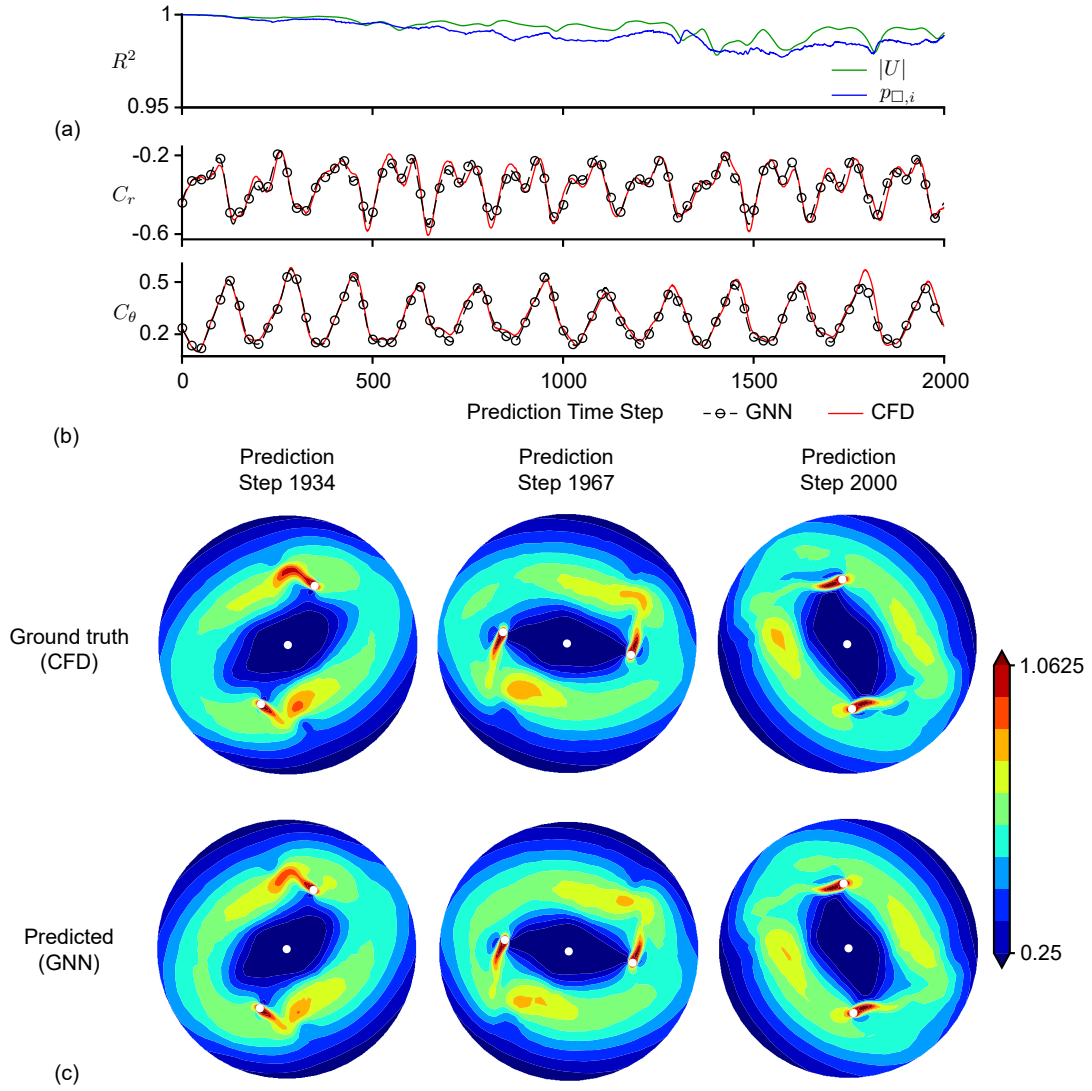


Figure 6: Results for the 2D test data set at $Re = 185$, where the flow is in transition from periodic to chaotic behavior. (a) Coefficient of determination between ground truth and predicted flow fields at every prediction time step, (b) lift and drag coefficients calculated from the ground truth and predicted flow fields for the cylinder marked in red in Fig. 2a at every prediction time step, (c) normalized velocity magnitude $|U|^*$ field at prediction time steps 1934, 1967, and 2000.

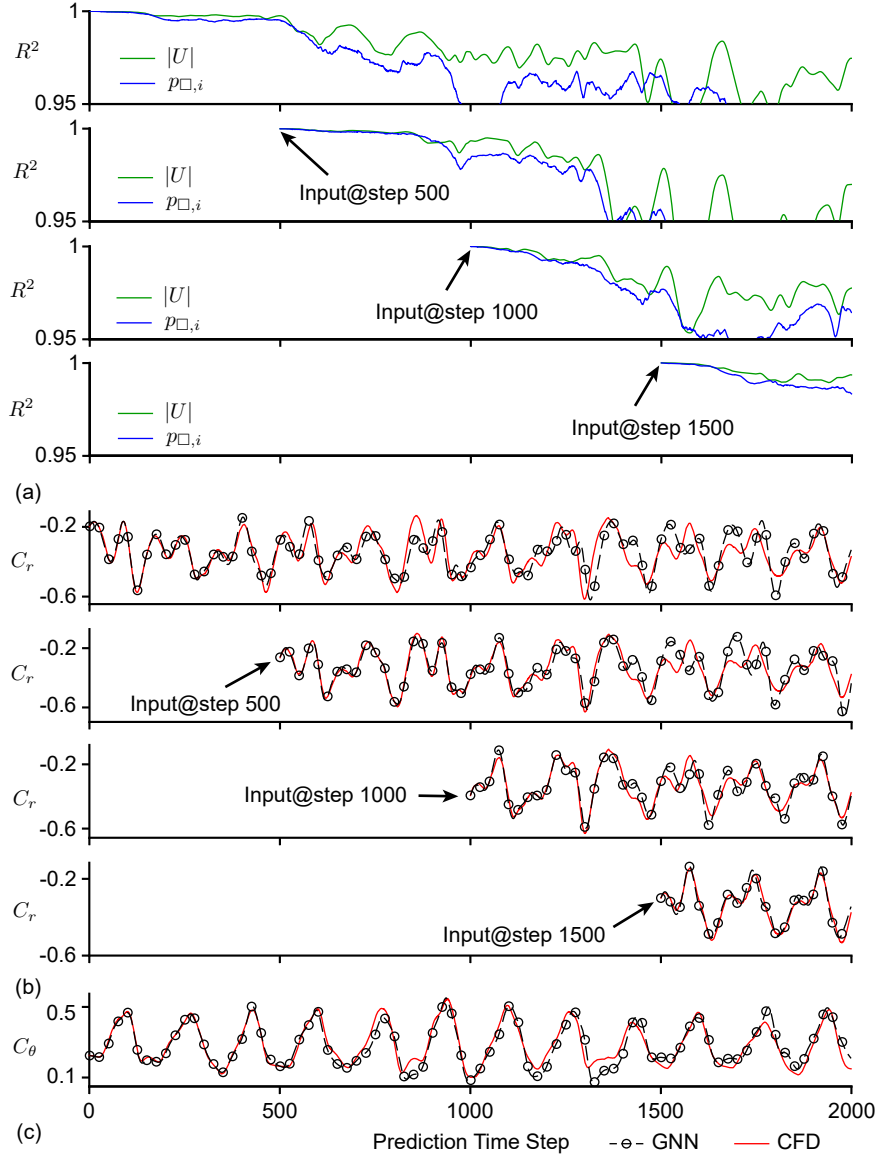


Figure 7: Results for the 2D test data set at $Re = 225$, where the flow displays chaotic behavior. (a) Coefficient of determination between ground truth and predicted flow fields at every prediction time step, starting from different time steps within the test data set, (b) lift coefficients calculated from the ground truth and predicted flow fields for the cylinder marked in red in Fig. 2a at every prediction time step, starting from different time steps within the test data set, and (c) drag coefficients calculated from the ground truth and predicted flow fields for one of the cylinders at every prediction time step.

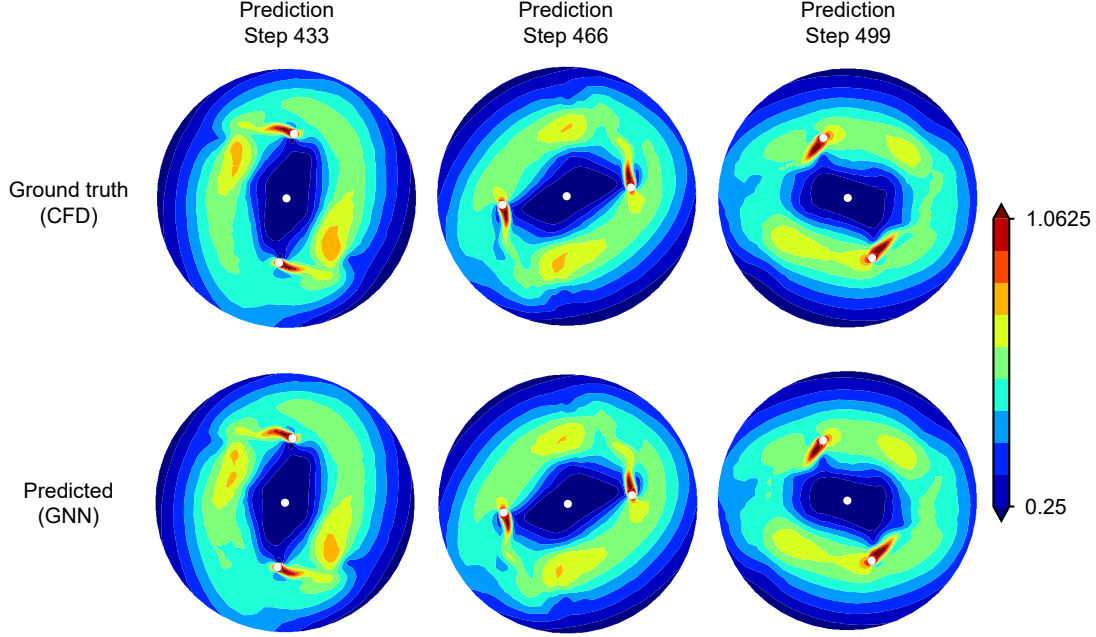


Figure 8: Normalized velocity magnitude $|U|^*$ field at prediction time steps 1934, 1967, and 2000 for the test data set at $Re = 225$ for the 2D chaotic flow case.

5. Conclusion

In this work, we proposed a hypergraph neural network (ϕ -GNN) framework for modeling unsteady fluid flow around rotating rigid bodies. By formulating the problem in corotating polar (2D) or cylindrical (3D) coordinate systems, the framework preserves rotation and translation equivariance with respect to the axis of rotation. This coordinate choice ensures consistency of the learned dynamics and enables effective modeling of flows around rotating structures. To handle domains without Dirichlet pressure boundaries, we proposed modeling the pressure fields indirectly through the construction and modeling of local directed pressure differences. This approach avoids ambiguity in absolute pressure values and enables reconstruction of the full pressure field via a linear system in post-processing. We also adopted the partitioning of hypergraphs and introduced a buffer construction approach that reduces memory overhead during training without hampering the accuracy of gradients. The proposed framework is applied to two test cases, namely the flow within a rotating mixer in 2D and the flow around a rotating cube in 3D. In both test cases, we observed that the framework is able to produce stable predictions for at least 2000 time steps, the predictions are accurate for periodic cases for at least 2000 time steps with minor accumulated phase error, and even for chaotic flow systems, the framework is still able to at least generate accurate predictions for 500 time steps. Accurate lift and drag force coefficients on the rotating body can be obtained via direct integration of the Cauchy stress tensor on the solid surface. In our future work, we plan to extend the application of the framework to fluid flow around more complex geometries like propellers and turbines.

Acknowledgment

This research is funded by the Natural Sciences and Engineering Research Council of Canada (NSERC) and Seaspan Shipyards. The generation of flow data sets was supported in part by computational resources and services provided by Advanced Research Computing at the University of British Columbia. Rui Gao thanks Nihar Darbhamulla and Biswajeet Rath for their help.

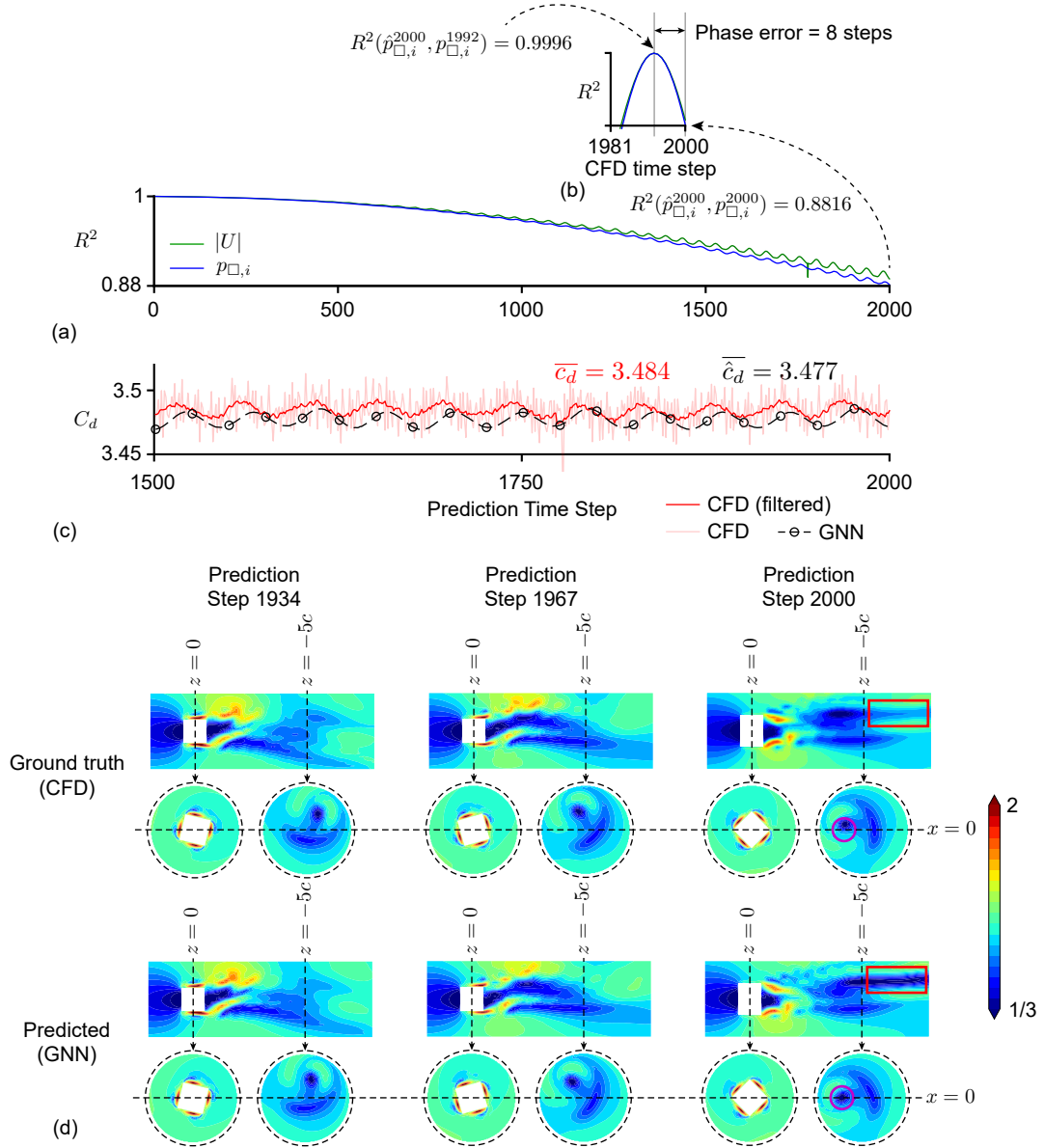


Figure 9: Results for the 3D rotating cube test case: (a) Coefficient of determination between ground truth and predicted flow fields at every prediction time step, starting from different time steps within the test data set, (b) coefficient of determination between predicted local directed pressure difference field $\hat{p}_{\square,i}$ at time step 2000 and ground truth local directed pressure difference field $p_{\square,i}$ at different time steps, which shows a accumulated phase error of about 8 time steps, (c) drag coefficients calculated from the ground truth and predicted flow fields between prediction time step 1501 and 2000, with the CFD drag force smoothed by a moving average filter of width 5, and (d) normalized velocity magnitude $|U|^*$ field from slicing plane $z = 0$, $z = -5c$, and $x = 0$ at prediction time steps 1934, 1967, and 2000.

References

- [1] H. Keck, M. Sick, Thirty years of numerical flow simulation in hydraulic turbomachines, *Acta mechanica* 201 (1) (2008) 211–229.
- [2] R. N. Pinto, A. Afzal, L. V. D’Souza, Z. Ansari, A. Mohammed Samee, Computational fluid dynamics in turbomachinery: a review of state of the art, *Archives of Computational Methods in Engineering* 24 (3) (2017) 467–479.
- [3] Z. Cheng, F.-S. Lien, E. Yee, H. Meng, A unified framework for aeroacoustics simulation of wind turbines, *Renewable Energy* 188 (2022) 299–319.
- [4] A. Posa, R. Broglia, M. Felli, M. Cianferra, V. Armenio, Hydroacoustic analysis of a marine propeller using large-eddy simulation and acoustic analogy, *Journal of Fluid Mechanics* 947 (2022) A46.
- [5] G. Li, H. Sun, J. He, X. Ding, W. Zhu, C. Qin, X. Zhang, X. Zhou, B. Yang, Y. Guo, Deep learning, numerical, and experimental methods to reveal hydrodynamics performance and cavitation development in centrifugal pump, *Expert Systems with Applications* 237 (2024) 121604.
- [6] C. Li, B. Liang, P. Yuan, Q. Zhang, Y. Liu, B. Liu, M. Zhao, Fast prediction of propeller dynamic wake based on deep learning, *Physics of Fluids* 36 (8) (2024).
- [7] X. Hou, X. Zhou, Y. Liu, Reconstruction of ship propeller wake field based on self-adaptive loss balanced physics-informed neural networks, *Ocean Engineering* 309 (2024) 118341.
- [8] F. Gao, Z. Zhang, C. Jia, Y. Zhu, C. Zhou, J. Wang, Simulation and prediction of three-dimensional rotating flows based on convolutional neural networks, *Physics of Fluids* 34 (9) (2022).
- [9] M. Zhang, L. Wang, Y.-B. Xu, X.-L. Wang, Rotating machinery flow field prediction based on hybrid neural network, *Journal of Turbulence* 25 (12) (2024) 482–500.
- [10] K. Liu, K. Luo, Y. Cheng, A. Liu, H. Li, J. Fan, S. Balachandar, Parameterized physics-informed neural networks (p-pinns) solution of uniform flow over an arbitrarily spinning spherical particle, *International Journal of Multiphase Flow* 180 (2024) 104937.
- [11] M. Zhang, C. Wang, J. Zhang, Performance prediction of co-rotating disk cavity with finned vortex reducer based on machine learning, *International Journal of Thermal Sciences* 205 (2024) 109287.
- [12] T. Pfaff, M. Fortunato, A. Sanchez-Gonzalez, P. W. Battaglia, Learning mesh-based simulation with graph networks, *arXiv preprint arXiv:2010.03409* (2020).
- [13] M. Lino, S. Fotiadis, A. A. Bharath, C. D. Cantwell, Multi-scale rotation-equivariant graph neural networks for unsteady eulerian fluid dynamics, *Physics of Fluids* 34 (8) (2022) 087110.
- [14] M. Lino, N. Thuerey, T. Pfaff, Se (3)-equivariant diffusion graph nets: Synthesizing flow fields by denoising invariant latents on graphs, in: *ICML 2024 AI for Science Workshop*, 2024.
- [15] M. Fortunato, T. Pfaff, P. Wirsberger, A. Pritzel, P. Battaglia, Multiscale meshgraphnets, *arXiv preprint arXiv:2210.00612* (2022).
- [16] Y. Cao, M. Chai, M. Li, C. Jiang, Bi-stride multi-scale graph neural network for mesh-based physical simulation, *arXiv preprint arXiv:2210.02573* (2022).
- [17] R. Gao, I. K. Deo, R. K. Jaiman, A finite element-inspired hypergraph neural network: Application to fluid dynamics simulations, *Journal of Computational Physics* (2024) 112866.

- [18] R. Gao, R. K. Jaiman, Predicting fluid–structure interaction with graph neural networks, *Physics of Fluids* 36 (1) (2024).
- [19] Z. Ma, Z. Ye, W. Pan, Fast simulation of particulate suspensions enabled by graph neural network, *Computer Methods in Applied Mechanics and Engineering* 400 (2022) 115496.
- [20] J. Xu, A. Pradhan, K. Duraisamy, Conditionally parameterized, discretization-aware neural networks for mesh-based modeling of physical systems, *Advances in Neural Information Processing Systems* 34 (2021) 1634–1645.
- [21] R. Gao, S. Heydari, R. K. Jaiman, Towards spatio-temporal prediction of cavitating fluid flow with graph neural networks, *International Journal of Multiphase Flow* 177 (2024) 104858.
- [22] S. Li, Z. Sun, Y. Zhu, C. Zhang, Physics-constrained and flow-field-message-informed graph neural network for solving unsteady compressible flows, *Physics of Fluids* 36 (4) (2024).
- [23] A. Kazadi, J. Doss-Gollin, A. Sebastian, A. Silva, Floodgnn-gru: a spatio-temporal graph neural network for flood prediction, *Environmental Data Science* 3 (2024) e21.
- [24] H. Tang, L. J. Durlofsky, Graph network surrogate model for subsurface flow optimization, *Journal of Computational Physics* 512 (2024) 113132.
- [25] Y. Zhao, H. Li, H. Zhou, H. R. Attar, T. Pfaff, N. Li, A review of graph neural network applications in mechanics-related domains, *Artificial Intelligence Review* 57 (11) (2024) 315.
- [26] J. Li, T. Liu, G. Zhu, Y. Li, Y. Xie, Uncertainty quantification and aerodynamic robust optimization of turbomachinery based on graph learning methods, *Energy* 273 (2023) 127289.
- [27] S. Barwey, R. Balin, B. Lusch, S. Patel, R. Balakrishnan, P. Pal, R. Maulik, V. Vishwanath, Scalable and consistent graph neural networks for distributed mesh-based data-driven modeling, in: *SC24-W: Workshops of the International Conference for High Performance Computing, Networking, Storage and Analysis*, IEEE, 2024, pp. 1058–1070.
- [28] S. Strönisch, M. Sander, M. Meyer, A. Knüpfer, Multi-gpu approach for training of graph ml models on large cfd meshes, in: *AIAA SCITECH 2023 Forum*, 2023, p. 1203.
- [29] P. Kakka, S. Nidhan, R. Ranade, J. F. MacArt, Sampling-based distributed training with message passing neural network, *arXiv preprint arXiv:2402.15106* (2024).
- [30] D. Dupuy, N. Odier, C. Lapeyre, D. Papadogiannis, Modeling the wall shear stress in large-eddy simulation using graph neural networks, *Data-Centric Engineering* 4 (2023) e7.
- [31] J. Murphy, Cfd simulation of flows in stirred tank reactors using a sliding mesh technique, in: *Instn. Chem. Engng. Symp. Ser.*, Vol. 136, 1994, pp. 341–348.
- [32] J. Han, Y. Rong, T. Xu, W. Huang, Geometrically equivariant graph neural networks: A survey, *arXiv preprint arXiv:2202.07230* (2022).
- [33] H. G. Weller, G. Tabor, H. Jasak, C. Fureby, A tensorial approach to computational continuum mechanics using object-oriented techniques, *Computers in physics* 12 (6) (1998) 620–631.
- [34] R. I. Issa, Solution of the implicitly discretised fluid flow equations by operator-splitting, *Journal of computational physics* 62 (1) (1986) 40–65.
- [35] A. Hölzer, M. Sommerfeld, New simple correlation formula for the drag coefficient of non-spherical particles, *Powder Technology* 184 (3) (2008) 361–365.

- [36] A. Haider, O. Levenspiel, Drag coefficient and terminal velocity of spherical and nonspherical particles, *Powder technology* 58 (1) (1989) 63–70.
- [37] P. Augier, A. V. Mohanan, C. Bonamy, FluidDyn: A python open-source framework for research and teaching in fluid dynamics by simulations, experiments and data processing, *Journal of Open Research Software* 7 (2019).
- [38] P. Virtanen, R. Gommers, T. E. Oliphant, M. Haberland, T. Reddy, D. Cournapeau, E. Burovski, P. Peterson, W. Weckesser, J. Bright, S. J. van der Walt, M. Brett, J. Wilson, K. J. Millman, N. Mayorov, A. R. J. Nelson, E. Jones, R. Kern, E. Larson, C. J. Carey, Í. Polat, Y. Feng, E. W. Moore, J. VanderPlas, D. Laxalde, J. Perktold, R. Cimrman, I. Henriksen, E. A. Quintero, C. R. Harris, A. M. Archibald, A. H. Ribeiro, F. Pedregosa, P. van Mulbregt, SciPy 1.0 Contributors, SciPy 1.0: Fundamental Algorithms for Scientific Computing in Python, *Nature Methods* 17 (2020) 261–272.
- [39] A. Paszke, S. Gross, F. Massa, A. Lerer, J. Bradbury, G. Chanan, T. Killeen, Z. Lin, N. Gimeshein, L. Antiga, et al., Pytorch: An imperative style, high-performance deep learning library, *Advances in neural information processing systems* 32 (2019).
- [40] V. Sitzmann, J. Martel, A. Bergman, D. Lindell, G. Wetzstein, Implicit neural representations with periodic activation functions, *Advances in Neural Information Processing Systems* 33 (2020) 7462–7473.
- [41] D. P. Kingma, J. Ba, Adam: A method for stochastic optimization, *arXiv preprint arXiv:1412.6980* (2014).
- [42] P. Micikevicius, S. Narang, J. Alben, G. Diamos, E. Elsen, D. Garcia, B. Ginsburg, M. Houston, O. Kuchaiev, G. Venkatesh, et al., Mixed precision training, in: *International Conference on Learning Representations*, 2018.